A99-33388 AIAA-99-3150

EFFECTS OF LEADING-EDGE ICE ACCRETION GEOMETRY ON AIRFOIL PERFORMANCE

Han S. Kim[*]
Michael B. Bragg[†]

University of Illinois at Urbana-Champaign

ABSTRACT

A systematic study of the effect of simulated ice shape geometry on airfoil aerodynamics was performed. A wind tunnel test was performed using a flapped NLF(1)-0414 airfoil where aerodynamic parameters including hinge moment were measured. The ice shapes tested were designed to simulate a single glaze ice horn with leading-edge radius, size and airfoil surface location varied. In all nine ice simulations were tested at six different leading edge locations. The objective of this research was to determine the sensitivity of iced airfoil aerodynamics to ice shape geometry. Configurations were also tested at three different Reynolds numbers (0.5, 1.0, and 1.8×10^6). It was determined that ice horn leading-edge radius had only a small effect on airfoil aerodynamics. However, the aerodynamic performance was very sensitive to ice shape size and location. An almost linear relationship between loss in maximum lift and ice horn location was found with the largest loss at the furthest location back on the upper surface. Reynolds number was found to have little effect on the aerodynamic results on the airfoil with simulated ice shapes.

INTRODUCTION

The term "critical ice accretion" is typically used to describe the one ice formation that is believed to cause the maximum degradation in aircraft performance. Critical ice accretions are currently used in the aircraft certification process. However, to accurately determine the critical ice accretion for an airfoil, the relationship between ice geometry, airfoil geometry, and corresponding performance degradation must be determined. This understanding is currently lacking. Determining this relationship also has other benefits, such as incorporating this relationship in the design phase of an airfoil or wings of an aircraft to minimize the sensitivity to icing. Also, the understanding of ice geometry vs. performance degradation may assist in improving the accuracy of computational models. This information will help determine when an ice shape is predicted with enough fidelity to properly simulate the aerodynamic effects of an actual ice accretion.

Large ice accretions effectively alter the gross airfoil geometry. The performance degradation trends consistent with large ice accretion can also be observed in variations in airfoil geometry. These effects of airfoil geometry are well documented by Hoemer and Borst.[1] The data presented as a function of nose radius, camber, and other variables, document their effect on airfoil aerodynamics and performance.

Taking a simplistic view of large ice accretion on airfoil geometry, the accretion can cause an increase in camber, changes in the airfoil nose radius, thickening of the airfoil, etc. Hoemer shows in detail the relationship between the parameters of an airfoil and their resulting performance effects. He states that leading-edge radius primarily determines the stall type and the $C_{\ell\,max}$ of an airfoil. Sharp leading edges generally result in thin airfoil or leading-edge stall, with lower $C_{\ell\,max}$ values.

---

[*] Graduate Research Assistant, Department of Aeronautical and Astronautical Engineering, Member AIAA.
[†] Professor and Head, Department of Aeronautical and Astronautical Engineering, Associate Fellow AIAA.

When the nose radius reaches about 1.5 to 2.0% of the chord, an optimum $C_{l\,max}$ results for most airfoils.

$C_{l\,max}$ and stall are also a function of camber. Hoerner states that camber allows laminar separation and the "bubble-plus-reattachment" mechanism to be minimized. He also states that these effects are relatively independent of the Reynolds number. Increases in camber generally result in corresponding increases in $C_{l\,max}$ until the camber becomes too great. So the effects of variations in camber resemble the effects of varying leading-edge radii. These effects correlate well to the effects of icing, which generally display losses in $C_{l\,max}$ and changes in stall types. However, it is important to note that this is a very simplistic view of large ice accretion, since the effect of ice accretion on the flowfield can not be simplified to just a gross variation in airfoil geometry.

Weick and Scudder[2] studied the effects of sharp leading edges on a Clark Y airfoil by attaching two different sharp leading-edge shapes. The tests showed that the sharp leading edges caused a slight reduction in drag, a change in stall type from a trailing edge stall to a more thin airfoil stall, and approximately 13% loss in $C_{l\,max}$. They also mention a similar Göttingen 398 test that showed a 26% decrease in $C_{l\,max}$ and a small negative lift curve slope post stall.

Ingelman-Sundberg, Trunov and Ivaniko's analysis provided a good starting point for this research. In their first joint report,[3] they tested various ice accretion shapes and sizes on a four-element, one-meter chord wing section, and on a 0.65-meter chord NACA 65_2A215 airfoil. They list the effects of large ice accretion on the airfoil flow:

1. Extracts kinetic energy from the boundary layer which promotes separation.
2. Causes increased local friction drag.
3. Reduces pressure recovery at the trailing edge.
4. Changes the wing section (effectively a geometry change of the wing section) and directly affects the pressure field.

The data showed that even the smallest ice accretion dramatically lowered the $C_{l\,max}$. They also noted that decrease in $C_{l\,max}$ with respect to size was nonlinear.

The data also suggested that the shape of the ice accretion and the surface condition of the airfoil had the most impact on the airfoil performance degradation, with rime ice shapes generally having less effect than horn-shaped ice of similar size. They also noted that the effects on $C_{l\,max}$ and C_d of ice accretion just on the lower surface was much less than when the accretion was placed on both upper and lower surfaces. The $C_{l\,max}$ loss was between 20 – 40% for cases with no trailing-edge devices and the $C_{l\,max}$ loss never exceeded 25% when trailing-edge devices were deployed. This study did not however discuss the effect of varying ice shape locations.

Ingelman-Sundberg and Trunov[4,5] showed large increases in elevator hinge moment caused by the redistribution of the pressure forces on the airfoil in their second and third joint report. Similar increases in hinge moment are thought to have caused numerous accidents, including the ATR-72 commuter aircraft accident of 1994 where the ice accretion caused a large hinge moment on the aileron.[6]

Mullins, Smith, and Korkan[7] showed that the chordwise location of residual ice shapes had a significant effect on the laminar bubble separation extent and reattachment. They also noted that separation without reattachment occurred when the ice shape was placed closer to the leading edge (x/c less than 10% chord on a NACA64A010 with k/c < 2.5%). This indicates that slight variations in the leading-edge geometry can have significant effects on the flowfield. They also suggested that adverse pressure gradients and the extent of laminar flow play an important part in airfoil performance in icing conditions.

Recent tests by Lee, et al.,[8] also show the importance of the chordwise position of an accretion representing a supercooled large droplet (SLD) accretion. A forward facing quarter round (.25", k/c = 0.0139) was tested on a modified NACA 23012 airfoil at varying chordwise locations. The iced cases showed a change in stall characteristics, dramatic reductions in $C_{l\,max}$ and large increases in drag. However, the worst case occurred when the simulated ice was near x/c = 0.10, where $C_{l\,max}$ decreased to 0.3 (80% decrease) compared to 0.56 for x/c = .02 (62% decrease), and 0.42 for x/c = 0.2 (72% decrease). The NACA23012 has a clean $C_{l\,max}$ of 1.4 at Re=1.5x10^6 and 1.48 at

Re=1.8x10^6. The x/c = 0.10 case also showed the worst drag increase and the lowest α_{stall} of just 6°. The pitching moments were also heavily dependent on the chordwise position.

Much of aircraft icing aerodynamics research to date has been limited by the lack of a clear understanding of the relationship between geometric parameters of ice accretion and their corresponding performance penalties. It is often though that ice shapes that are similar in size but of different geometry can have vastly differing effects on airfoil performance. Also, current belief is that when an accretion grows sufficiently large, any additional increase in size no longer has an effect on the $C_{l\ max}$. It is desired to investigate the aerodynamic effects caused by these large ice accretions in order to explain or contradict these assumptions. Understanding the relationship between ice accretion geometry and the resulting aerodynamic penalty is also important in establishing procedures to determine the most critical ice accretion geometry. This experimental study focuses primarily on the relationship between airfoil leading-edge ice geometry (ice accretion height, horn radius, and location) and aerodynamic performance.

EXPERIMENTAL SETUP

A scaled drawing of the simulated ice and the model is shown in Fig. 1. An 18-inch chord NLF(1)-0414 was used for this research. The simulated ice shapes were machined out of aluminum and attached to the model via model end plates and secured with tape. For the larger shapes, the gaps between the base of the simulated ice shapes and the surface of the model were filled with plastina (modeling clay). The simulations maintained constant size and shape over the entire span. The simulated ice was tested in 3 sizes: k = 1.2" (k/c = 6.67 %), k = 0.8" (k/c = 4.44%), and k = 0.4" (k/c = 2.22%). The simulated ice shapes were tested at six different surface locations. The locations and horn angles are shown in Fig. 2. The ice shapes were attached normal to the surface at those locations. It can be seen in Table 1 that the locations were chosen so that each subsequent location doubles the horn angle and doubles the distance for both upper and lower surfaces. The horn angle was measured from the model chord

line to the line connecting the mid point of the base to the tip of the ice simulation. The simulated ice geometries were determined from averaging geometry data from a set of actual ice accretions collected from a test at the NASA Lewis Icing Research Tunnel. Due to geometric differences between the upper and lower surface ice, only upper surface ice accretion geometries were simulated for this research, although these geometries were also tested at two lower surface locations. As of this writing no two-horn (both upper and lower horns) configurations have been tested, but these tests will be conducted in the near future. The ice shapes used can be found in Shin and Bond[9] and an example is given in Fig. 3.

The research was performed in the UIUC 3 x 4 ft. wind tunnel. Figure 4 shows the schematic of the experimental setup. Each configuration was tested at two Reynolds numbers (1.0 x 10^6 and 1.8 x 10^6) and 3 flap settings (-5°, 0°, and 5°). C_l and C_m about c/4 were mainly taken from the force balance and C_d values were calculated primarily from the wake although force balance data were also collected. Surface pressure measurements were taken over areas which were not covered by the ice simulations, and C_h was calculated from a hinge moment load cell and surface pressure. Figure 4 shows the experimental setup. Florescent oil flow-visualization tests were also performed to determine and verify flow characteristics. All data shown are corrected for tunnel wall effects via methods described in Rae and Pope.[10]

RESULTS AND DISCUSSION

Simulated Ice Leading-Edge Radius

Figure 5 shows the C_l vs. α curves for k = 0.8" and s/c = 1.7% with varying horn tip radii. The ice simulations cause the $C_{l\ max}$ to decrease from the clean value of 1.35 to about 0.76 ($C_{l\ max}$ = 0.79 for r/w=.5, $C_{l\ max}$ = 0.75 for r/w = 0). Figure 6 shows the C_l vs C_d curves from the same data set as Fig. 5. A drag increase for the airfoil with simulated ice shapes can clearly be observed when compared to the clean case, but the simulated ice horn leading-edge radius has negligible effect on the data. All three ice shapes show a C_{dmin} value of about 0.014 (at C_l = .6) compared to .007 (at C_l = 0.68) for the clean airfoil, and the curves

for the three ice shapes are virtually identical. Figure 7 shows the C_m vs α curves for the same data set. Again it can be observed that the affect of the simulated ice leading-edge radius plays only a small role in determining airfoil performance parameters. The addition of the ice shapes caused the airfoil to have a more nose up pitching moment (increase in C_m) but the magnitude of this change was not affected by the ice simulation leading-edge radius.

The magnitude of the ice simulation leading-edge radius effect varied slightly with position and height. Ice leading-edge radius effects were most pronounced near and post stall for larger simulated ice shapes and positions further away from the leading edge. The sharper shapes (lower r/w) displayed lower $C_{\ell max}$ values but generally lower C_{dmin} values as well. Leading-edge radius effects on C_m were also minimal. As shown in Figs. 5, 6, and 7, the magnitude of the differences were less than 5% of the average values at a point.

Simulated Ice Height

The effect of height was strongly dependent on the surface position of the simulated ice. Figures 8 and 9 show the C_ℓ, C_m, and C_d curves with the simulated ice at s/c = 0% and Re=1.8x10^6 and Figs. 10 and 11 show the same at s/c = 3.4%. As shown in Fig. 8, height variations near the leading edge did not cause any appreciable change in $C_{\ell max}$ which remains near 1.1 regardless of height variations ($C_{\ell max}$ = 1.12 for k = 0.4", $C_{\ell max}$ 1.09 for k = 0.8", $C_{\ell max}$ = 1.10 for k = 1.2"). The same is true for α_{stall} which remains near α = 9°-10°. However, it can be seen that there is a large incremental change in C_m caused by the variation in height, with the moment increasing as the ice height increases for 0° < α < 10°. Near α = 9° the k = 1.2" shape shows C_m = -.005, k = 0.8" shows C_m = -.013, and k = 0.4" shows C_m = -.031. This is probably due to the changes in the flowfield and the effective lengthening of the airfoil chord due to presence of the ice shape. Extending the leading edge increases the ice shape moments and this coupled with the larger force on the larger shape increases the C_m about the quarter chord location. This is also unusual since changes in C-$_m$ generally indicate changes in the flowfield which are also reflected in C_ℓ. However, this is not the case here as seen in the two figures.

It's also interesting to note that the C_{dmin} for the largest and smallest shape (k = 0.4" and 1.2") are less than that for the medium size shape (k = 0.8") although the overall C_d values are in logical order at higher α's. This may be due to the base width of the ice shape. The k = 0.4" shape's base width account for only a fraction of the airfoil's thickness near the leading edge, which accounts for it's negligible effect on drag. The k = 1.2" shape is very close to the thickness of the airfoil near the leading edge which allowed the gap between the base of the ice shape and the airfoil to be sealed relatively smooth (essentially acting as a fairing). For the k = 0.8" shape, this was not the case. This probably caused a separation bubble to form which altered the local and possibly the global flowfield. A drawing of the three shapes in this configuration can be seen in Fig. 12.

At s/c = 3.4%, the height makes a significant difference in $C_{\ell max}$ and α_{stall} as shown in Fig. 10. With k = 1.2", the $C_{\ell max}$ = .43 and α_{stall} = 1°, which is only about 32% of the clean $C_{\ell max}$ and 12° less than the clean α_{stall}. The k = .8" and k = .4" shapes show $C_{\ell max}$ values of .56 and .72, respectively and α_{stall} values of 3° and 5°, respectively. It is interesting to note that the although the angle at which the peaks in C_m occur are very different from s/c = 0%, the magnitude of the change in C_m in Fig. 8 are similar to the magnitudes seen at Fig. 10. Figure 10 also seems to show a change in stall type from the trailing-edge stall type of the clean configuration to a more thin-airfoil stall type for the simulated ice configurations. Figure 11 shows that C_d increases roughly proportional to height, but C_{dmin} for k = 0.8" and 1.2" were the same with a value of C_{dmin} = .02 (although they occur at different C_ℓ's).

Simulated Ice Surface Position

As implied previously, surface position plays a critical role in the aerodynamic performance degradation due to icing. Effects of varying surface positions on C_ℓ, C_d, C_m, and C_h are given in Figs. 13, 14, 15 and 16. It can be seen that larger s/c locations cause a larger decrease in $C_{\ell max}$ and lower α_{stall} as compared to the clean case. $C_{\ell max}$ values in Fig. 13 are 1.36, 1.26, 1.09, 0.93, 0.80 and 0.63 (ice shape location s/c= -1.2% to 3.4% listed in increasing s/c) compared to 1.35 for the clean case. When attached to the lower surface, the

simulated ice provided slightly higher than the clean positive $C_{\ell\,max}$ values with the simulated ice essentially acting as a leading-edge flap. It also should be noted that as ice shape location s/c increases, the C_{dmin} values occur at lower C_ℓ's or lower α's.

Figure 14 shows that $C_{dmin} \cong .016$ for all s/c locations except for the s/c = 3.4% position which had $C_{dmin} = .021$, which was unexpected. All ice shape locations produced C_{dmin} values higher than clean values. However, as shown in Fig. 9, C_{dmin} values close to the clean values are possible. It also should be noted that as s/c increases, the C_{dmin} values occur at lower C_ℓ's and lower α's. These results seem to support the idea that iced airfoil drag is lowest at the angle of attack the ice was accreted at (α_{iced}). It also suggests that the vicinity of s/c = 3.4% may represent the limit as to what can be categorized as a "leading-edge" ice accretion for this airfoil. A similar effect has been seen in other research with SLD shapes.[8] This point has important implications and need additional research.

Figure 15 shows that the C_m values near positive stall for ice simulations occur at fairly even increments of α as s/c decreases from 3.4% to 0%. The breaks occur with a difference of 2° to 3° between these cases. C_m values for the upper surface iceshape locations at α's near positive stall remain fairly constant with $C_m \cong -.02$. C_m quickly decreases with an increase in α after stall to create a more nose down pitching moment. A similar angle effect occurs for the negative stall region in the cases where the ice simulations are placed on the lower surface (s/c $\leq$ 0) although the magnitude of C_m decreases as the ice simulation is moved further aft on the lower surface.

Figure 16 shows that the C_h values with simulated ice remain similar to clean configuration values until α approaches α_{stall}. C_h slightly increases above clean values just before stall and then sharply decreases below clean values after stall causing a sharp flap trailing edge up moment. For example, with simulated ice placed at the s/c = 0% location, $C_h = -0.12$ at $\alpha = 7°$ compared to the clean configuration value of $C_h = -0.14$. At $\alpha_{stall} = 10°$, the two values become similar as the hinge moment for the iced configuration becomes more negative (clean configuration $C_h = -0.16$, simulated ice $C_h = -0.156$). At $\alpha = 12°$, the simulated ice $C_h = -0.20$ compared to clean configuration value of

$C_h = -0.164$.

Figures 17, 18, and 19 show linear fits of $C_{\ell\,max}$ plotted against simulated ice surface position for k = 0.4", 0.8" and 1.2", respectively. The line averages the data set from all three radii. The incremental decrease in $C_{\ell\,max}$ with increase in surface position can be readily observed by the negative slope. The height effect can also be observed by comparing the three figures since the slopes become more negative as height increases. Figure 20 combines the linear curve fits from the 3 data sets. This plot shows that s/c near 0.4% exhibit negligible sensitivity to ice accretion height. Some believe that when an accretion grows sufficiently large, further increase in ice shape size does not increase the aerodynamic degradation further. Figure 20 shows that this may be true for ice accreted near a s/c location of 0.4%. However, it can also be seen from Fig. 20 that at s/c locations near 3.4% and -1.2%, $C_{\ell\,max}$ can be affected by changes in simulated ice height. At this point, it is not possible to conclude that the relationship illustrated in Fig. 20 is universal for other ice horns on airfoils.

Figures 17, 18 and 19 also show the effect of ice horn leading-edge location relative to s/c location. The values between the 3 radii on Fig. 17 are similar at all s/c locations tested. However, on Figs. 18 and 19, the values between the 3 radii grow further apart as s/c moves away from s/c = 0.4%. In Figure 19, s/c=3.4% shows a ΔC_{lmax} of .15 between r/w = 0 and r/w = 0.5. These plots show that ice simulation geometry becomes more important as s/c moves further away from s/c=0.4%.

One factor that is missing from this test is the effect of horn angle. It is also impossible for this relationship (Fig. 20) to remain linear for all s/c locations since $C_{\ell\,max}$ would have to continue to decrease as the ice shape is moved further aft resulting in impossibly high (or low) $C_{\ell\,max}$ values.

Reynolds Number Effects

Figures 21 and 22 show the clean airfoil data for the NLF 0414 at Reynolds Numbers of 0.5×10^6, 1.0×10^6, 1.8×10^6. It can be seen from Fig. 21 that $C_{\ell\,max}$ varies greatly with Reynolds Number. The $C_{\ell\,max}$ for 0.5×10^6 case was 1.12 whereas $C_{\ell\,max}$ for 1.8×10^6 case was 1.35; a difference of 0.23. It can also be seen from Fig. 22 that the drag polar shifts to the right (increased

drag at the same lift coefficient) with decreasing Reynolds Number. With the addition of simulated ice, the Reynolds Number effect was greatly reduced. This can be seen in Figs. 23 and 24. Figure 23 shows that C_l and C_m between the three Reynolds Numbers tested are virtually identical. The $C_{l\,max}$ for 0.5×10^6 case was 1.10, 1.0×10^6 case was 1.12, and for 1.8×10^6 case was 1.09; a maximum difference of 0.03. Therefore, $\Delta C_{l\,max}$ between clean and iced configurations may vary with Reynolds Number, but the actual $C_{l\,max}$ of the ice shape can be reproduced correctly at least within this Reynolds Number range.

CONCLUSIONS

The results to date indicate that ice surface location combined with ice horn height play a crucial role in determining iced airfoil performance degradation. It also seems that the size of the ice accretion, even when sufficiently large, does not alone determine the "critical" ice shape. Specific conclusions are:

- Simulated ice shape size and location had a significant effect on the measured reduction of $C_{l\,max}$ and other measures of aerodynamic performance.
- The relationship between surface location and $C_{l\,max}$ near the leading edge (x/c < 3.5%) is fairly linear with $\Delta C_{l\,max}$ increasing as the ice shape is placed further aft on the airfoil upper surface.
- $C_{l\,max}$ dependence on ice simulation height and radius was a minimum at s/c = 0.4%
- Reynolds Number had little effect on the $C_{l\,max}$ of the airfoil with simulated ice horns.
- Radius effects are largest for large horns at large s/c locations but are small compared to size and location effects.
- Drag results seem to support the idea that iced airfoil drag is lowest at the angle of attack the ice was accreted at (α_{iced}).
- Drag results also suggest that the vicinity of s/c = 3.4% may represent the limit as to what can be categorized as a "leading-edge" ice.

References:

[1] Hoerner, S. F. and Borst, H. F. Fluid-Dynamic Lift, Hoerner Fluid Dynamics, Brick Town, N.J., 1975.

[2] Weick, Fred and E. Scudder, Nathan F., "The Effect on Lift, Drag, and Spinning Characteristics of Sharp Leading Edges on Airplane Wings", NACA TN 447, February 1933.

[3] Ingelman-Sundberg, M., Trunov, O.K. and Ivaniko, A., "Methods for Prediction of the Influence of Ice on Aircraft Flying Characteristics", a joint report from the Swedish-Soviet Working Group for Flight Safety, 6th Meeting, 1977.

[4] Ingelman-Sundberg, M. and Trunov, O.K. "Wind Tunnel Investigation of the Hazardous Tail Stall Due to Icing", a joint report from the Swedish-Soviet Working Group for Flight Safety, 1979.

[5] Ingelman-Sundberg, M. and Trunov, O.K. "On the Problem of Horizontal Tail Stall Due to Ice", a joint report from the Swedish-Soviet Working Group for Flight Safety, 1985.

[6] Bragg, M.B. "Aircraft Aerodynamic Effects Due to Large Droplet Ice Accretions", AIAA 96-0932, January 1996.

[7] Mullins, B. Jr., Smith, D., and Korkan, K. "Effects of icing on the Aerodynamics of a Flapped Airfoil", AIAA 95-0449, January 1995.

[8] Lee, S., Dunn, T., Gurbacki, H. M., Bragg, M. B., and Loth, E., "An Experimental and Computational Investigation of Spanwise-Step-Ice Shapes on Airfoil Aerodynamics", AIAA 98-0490, January, 1998.

[9] Shin, Jaiwon, and Bond, Thomas H., "Repeatability of Ice Shapes in the NASA Lewis Icing Research Tunnel", *Journal of Aircraft*, Vol. 31, No. 5, Sept-Oct. 1994.

[10] Rae, W. H. and Pope, A., Low-Speed Wind Tunnel Testing, John Wiley & Sons, 1984.

Table 1: Simulated Ice Locations and Angles Tested

% s/c	Surface Positions Tested					
% s/c	3.4	1.7	0.85	0	-0.6	-1.2
θ (°)	60	40	20	0	-25	-50

k/c = 6.67%   k/c = 4.33%   k/c = 2.00%   Smaller shapes are approximately 2/3 and 1/3
w/c = 3.47%   w/c = 2.26%   w/c = 1.04%   scale of the largest shape.

105°   radius: sharp

99°   radius: 25% of base width
                                                max radius: 0.1531 in. (r/c = .85%)

k=1.2 in   ⌐k=0.78 in
                            ⌐k=0.36 in   radius: 50% of base width
                                            max radius: .3062 in. (r/c = 1.70%)

—w=0.625in—   —w=0.406in—   —w=0.188in—

k=1.2 in
60°   s/c=3.4%   NLF(1)-0414F
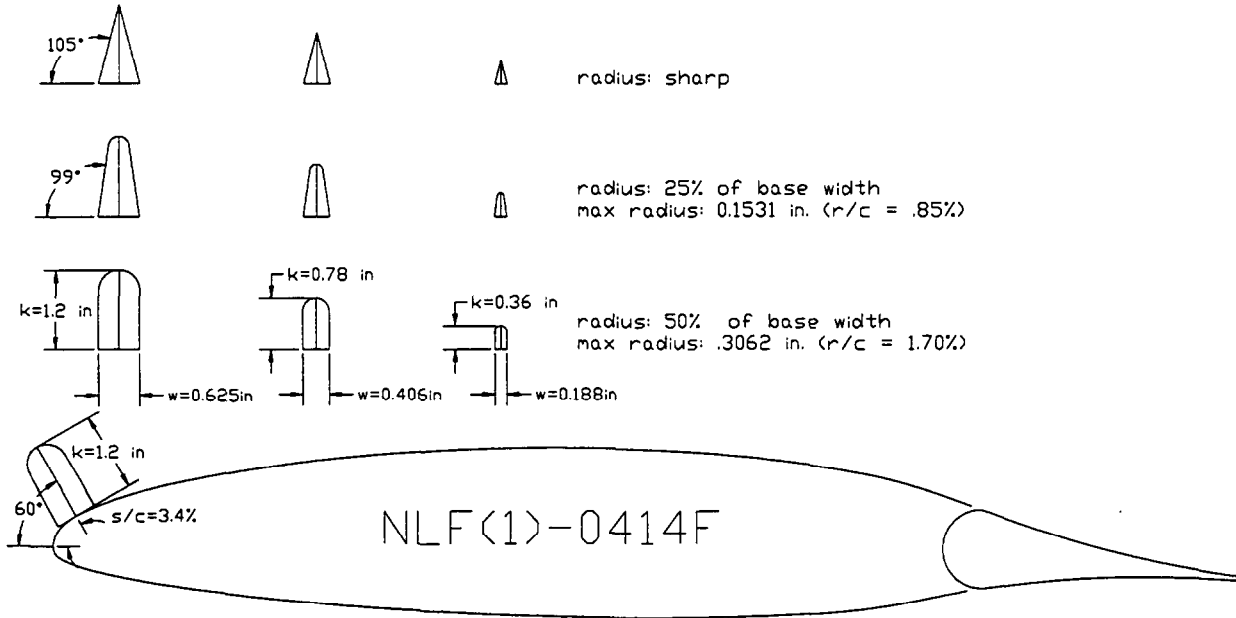
Figure 1: Simulated Ice Shapes and NLF-0414 Model

s/c = 3.4%, 60 degrees   s/c = 0%, 0 degrees

s/c = 1.7%, 40 degrees   s/c = -0.60%, -25 degrees

s/c = 0.85%, 20 degrees   s/c = -1.2%, -50 degrees
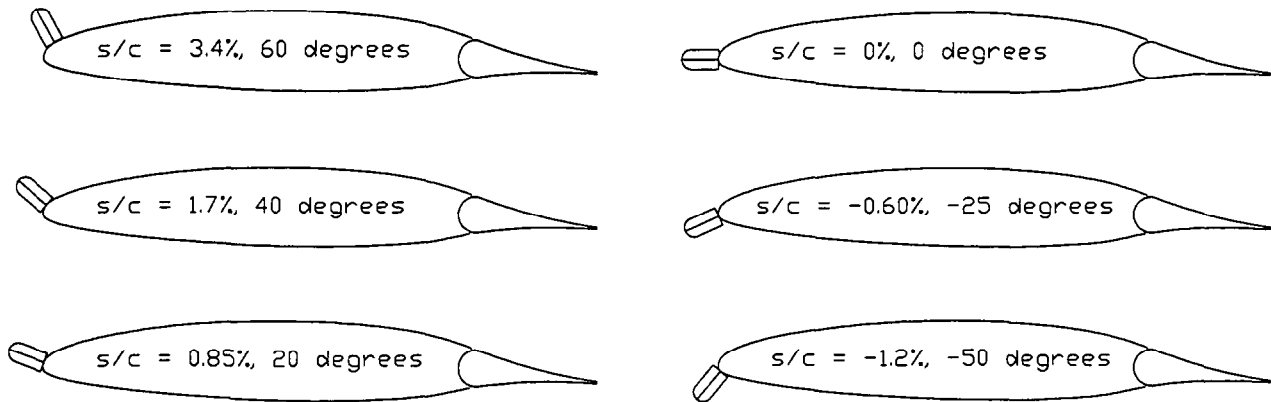
Figure 2: Simulated Ice Shape Locations and Angles

385
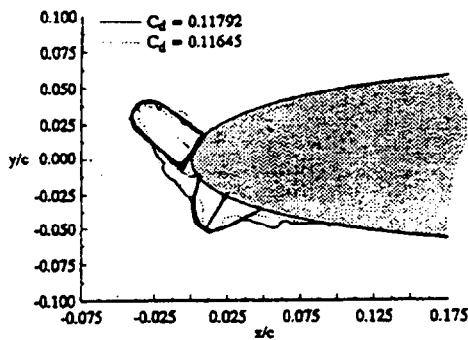
Figure 3: Ice Shape from Shin and Bond.[9] $\alpha = 4°$, LWC = 1.0 g/m^3, MVD = 20 µm, t = 12 min, V_x = 150 mph, $T_t = 28°$ F
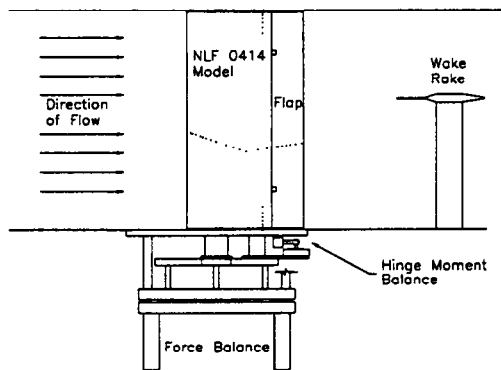
Figure 4: Schematic of the Experimental Setup
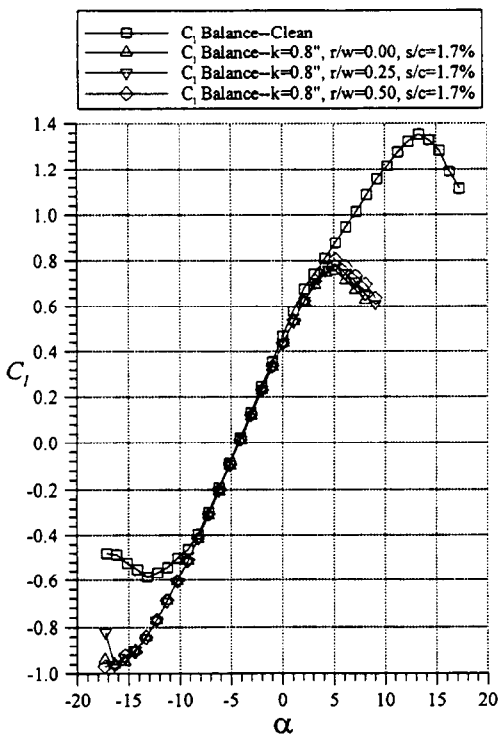
Figure 5: Ice Simulation Leading-Edge Radius Effects on C_l
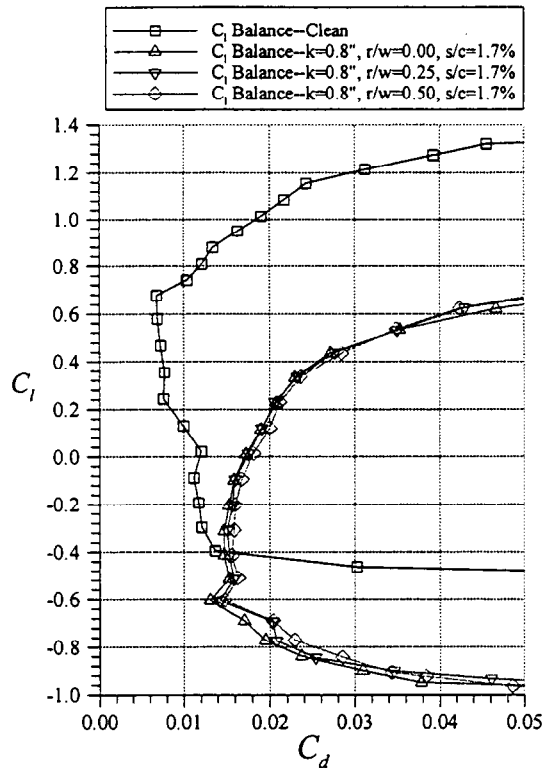
Figure 6: Ice Simulation Leading-Edge Radius Effects on C_d
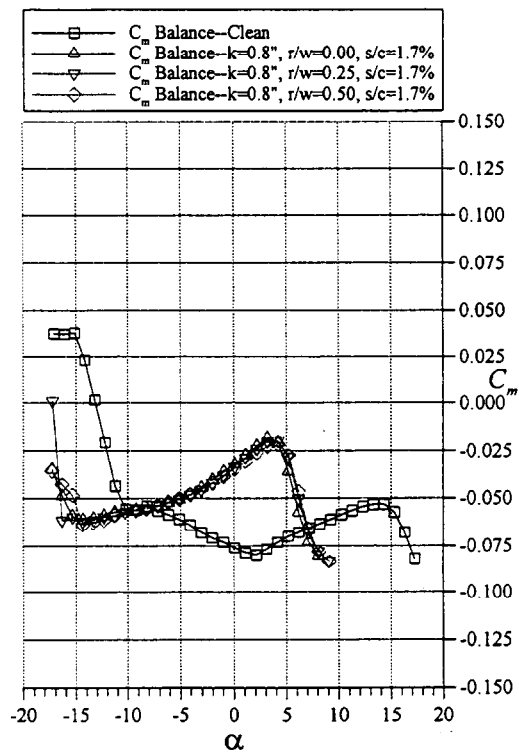
Figure 7: Ice Simulation Leading-Edge Radius Effects on C_m

386
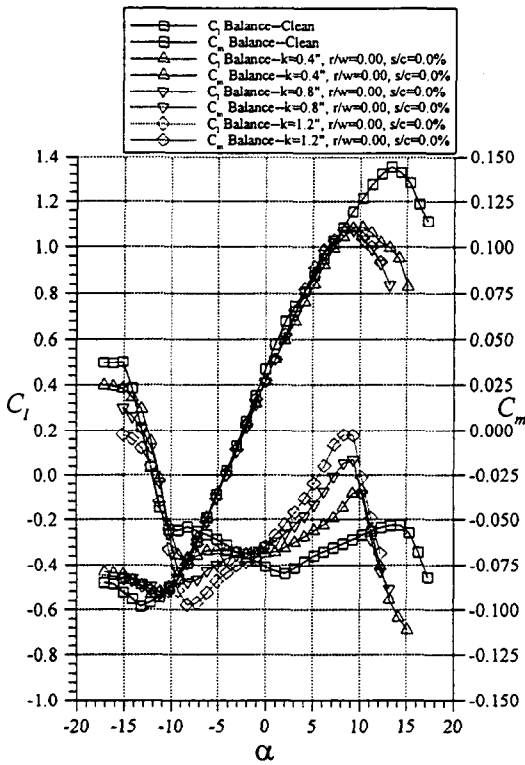
Figure 8: Ice Simulation Height Effects on C_l and C_m at s/c = 0%. Re=1.8x10^6
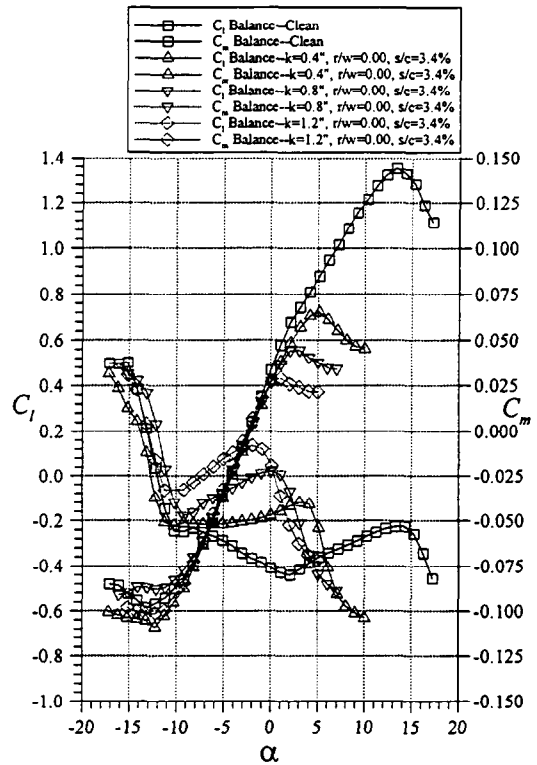
Figure 10: Ice Simulation Height Effects on C_l and C_m at s/c = 3.4%. Re=1.8x10^6
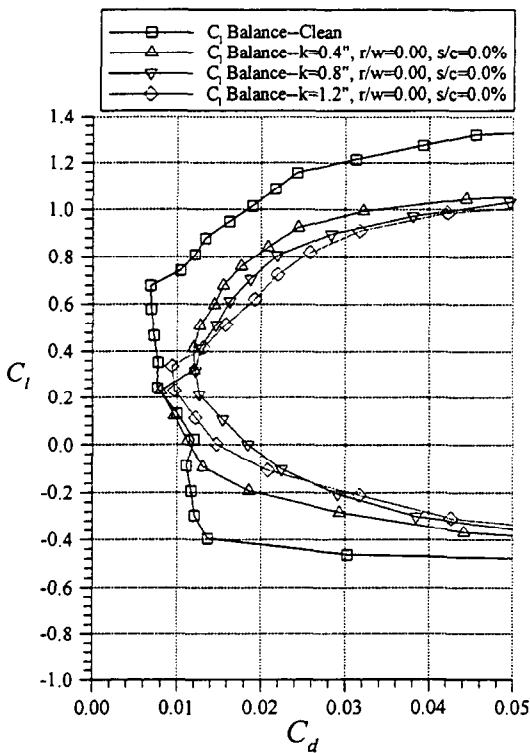
Figure 9: Ice Simulation Height Effects on C_d at s/c = 0%. Re=1.8x10^6
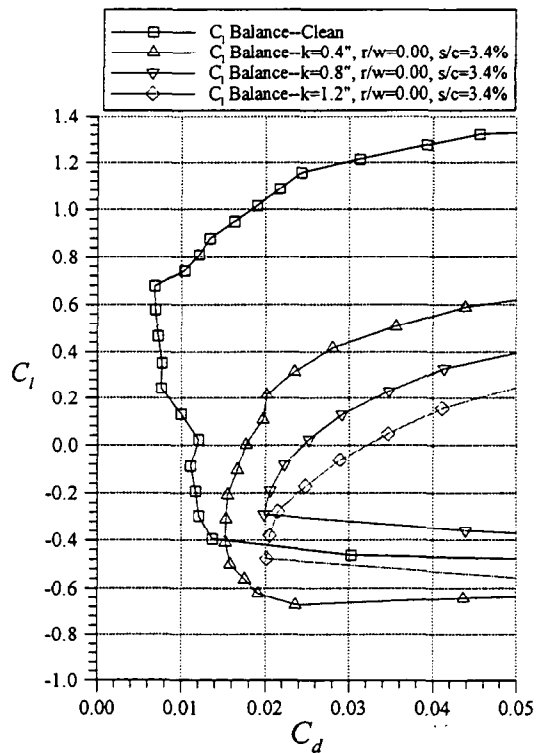
Figure 11: Ice Simulation Height Effects on C_d at s/c = 3.4%. Re=1.8x10^6

387
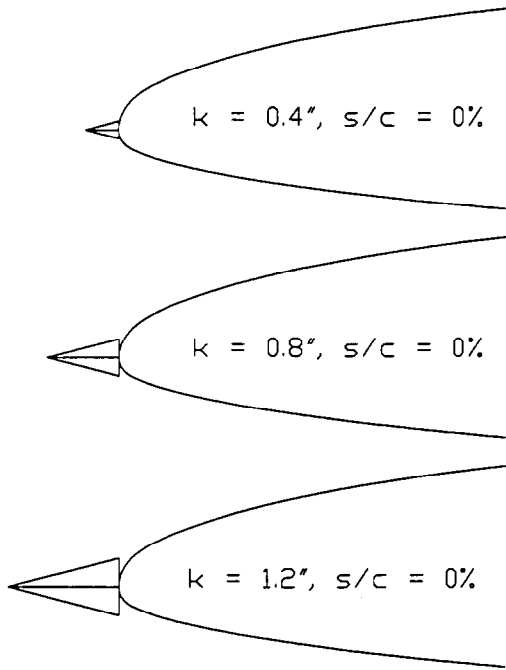
Figure 12: Three r/w = 0 ice simulations placed at s/c = 0%
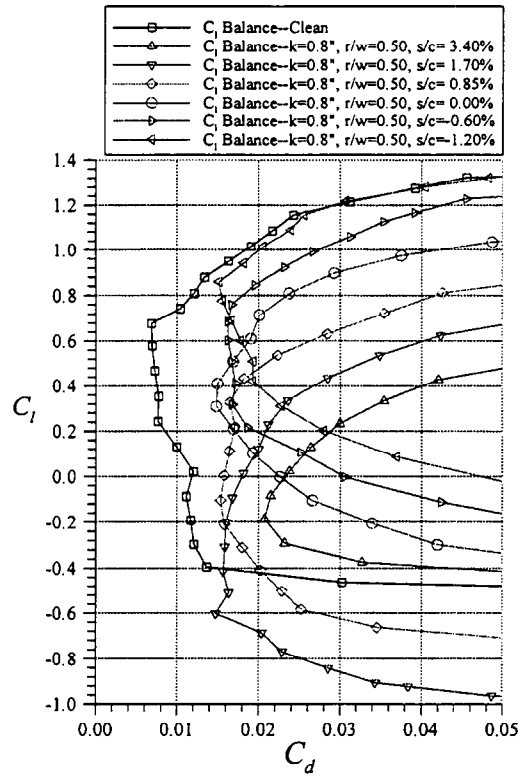
Figure 14: Position Effects on C_d for r/w = 0.5 and k = 0.8" shape. Re=1.8x10^6
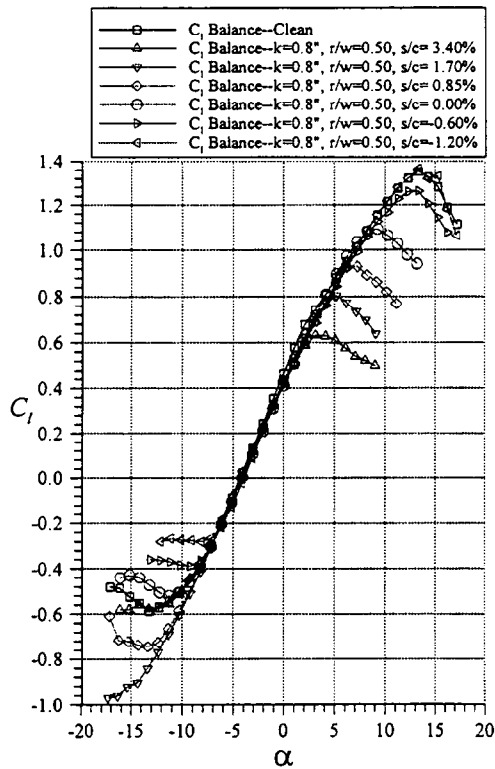
Figure 13: Position Effects on C_l for r/w = 0.5 and k = 0.8" shape. Re=1.8x10^6
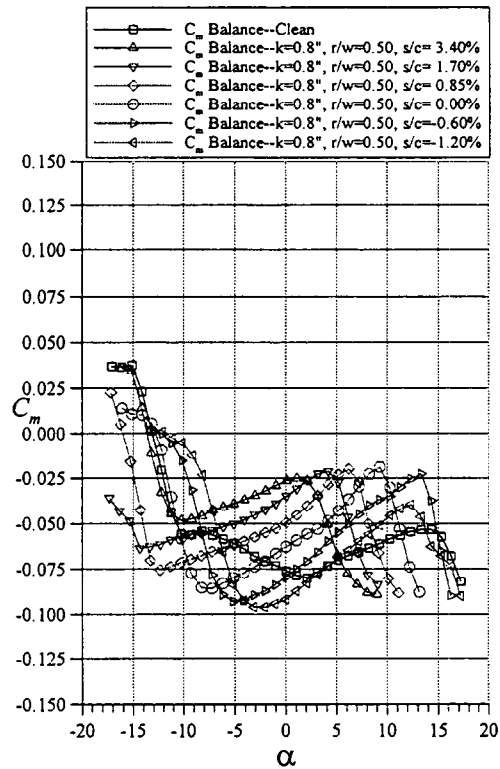
Figure 15: Position Effects on C_m for r/w = 0.5 and k = 0.8" shape. Re=1.8x10^6

388
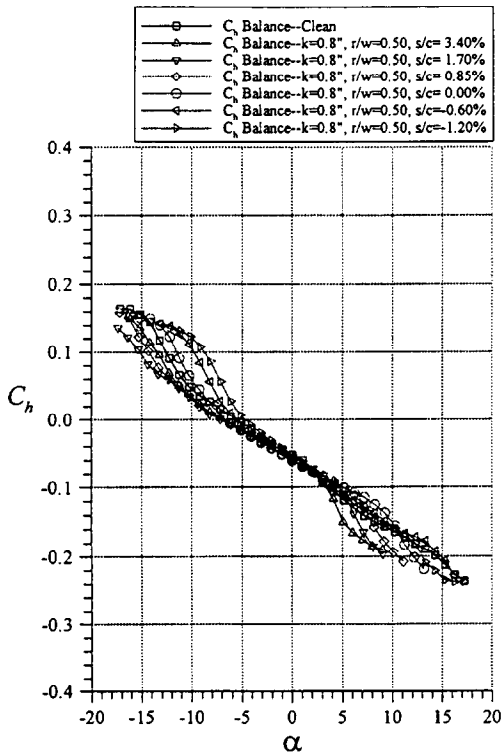
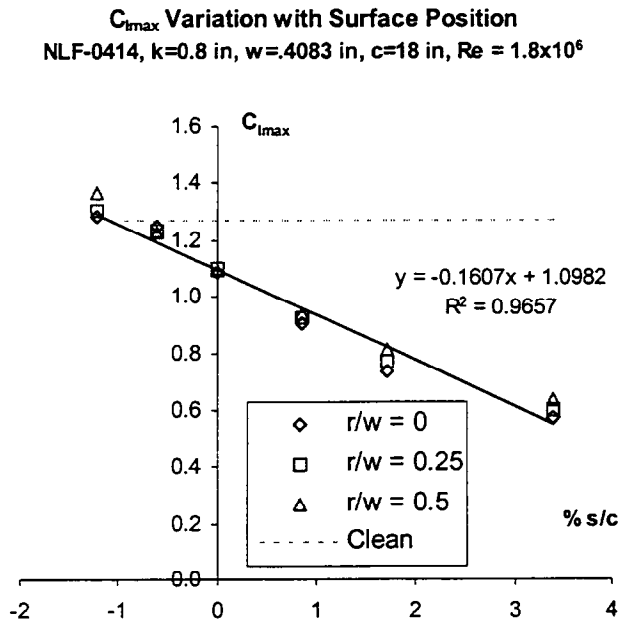**Figure 16:** Position Effects on C_h for r/w = 0.5 and k = 0.8" shape. Re=1.8x10⁶

C_{lmax} Variation with Surface Position
NLF-0414, k=0.8 in, w=.4083 in, c=18 in, Re = 1.8x10⁶

$$y = -0.1607x + 1.0982$$
$$R^2 = 0.9657$$

Figure 18: C_{lmax} vs. Surface Position for k = 0.8 in shape

C_{lmax} Variation with Surface Position
NLF-0414, k=0.4 in, w=.2042 in, c=18 in, Re = 1.8x10⁶

$$y = -0.1177x + 1.1091$$
$$R^2 = 0.9767$$
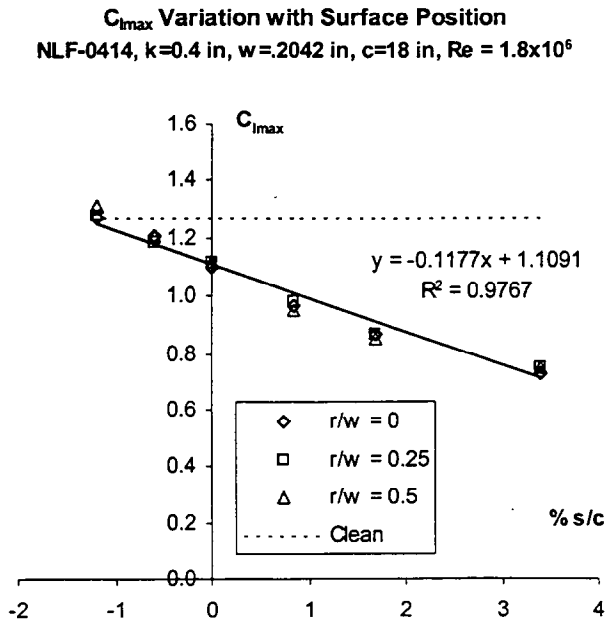
Figure 17: C_{lmax} vs. Surface Position for k = 0.4 in shape

C_{lmax} Variation with Surface Position
NLF-0414, k=1.2 in, w=.6125 in, c=18 in, Re = 1.8x10⁶

$$y = -0.2004x + 1.1079$$
$$R^2 = 0.9803$$
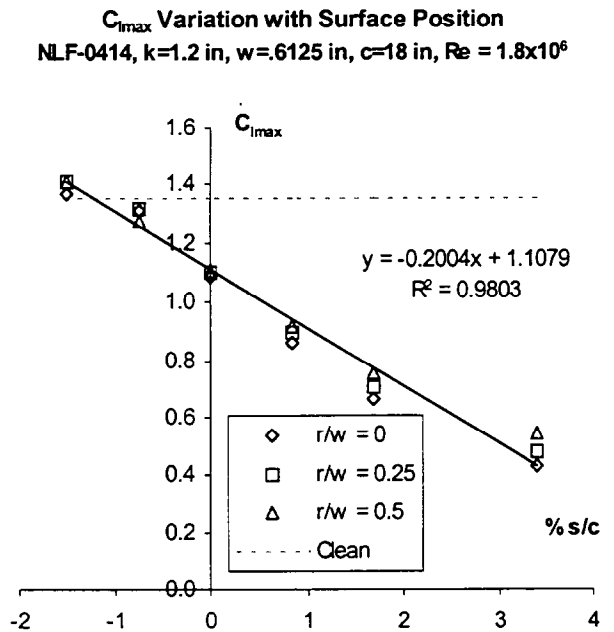
Figure 19: C_{lmax} vs. Surface Position for k = 1.2 in shape

389

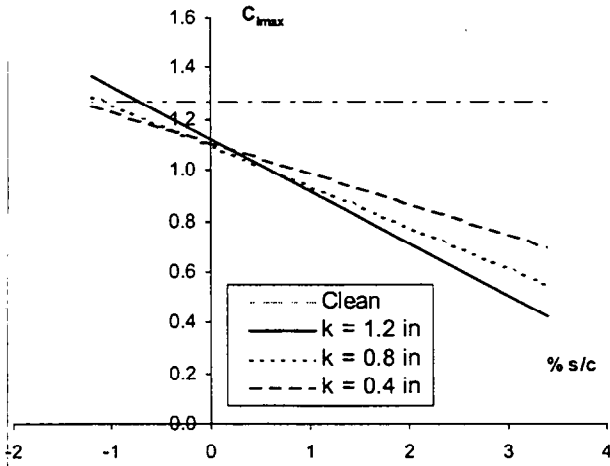C_{lmax} Variation with Surface Position Linear Curve Fits

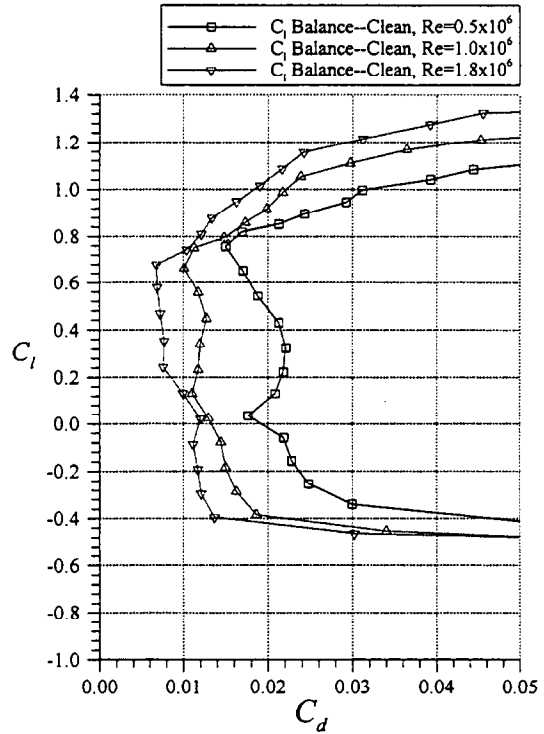**Figure 20:** Linear Fits from Figures 16, 17 and 18
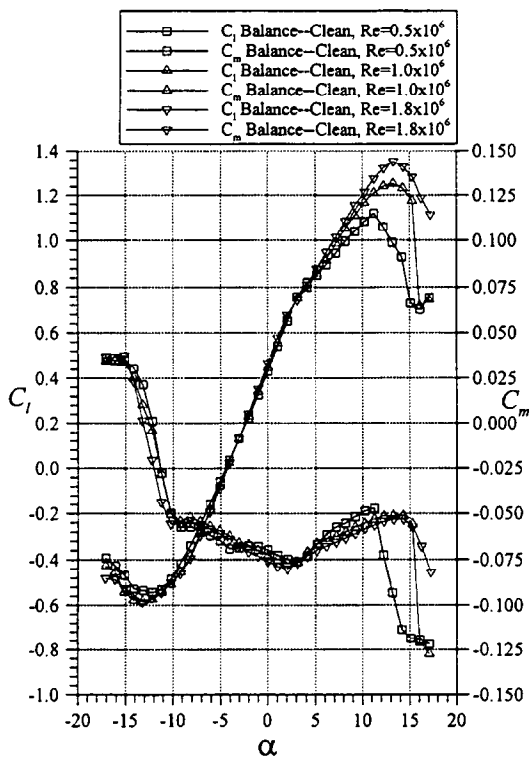

Figure 22: NLF0414 Clean Airfoil Data at 3 Reynolds Numbers

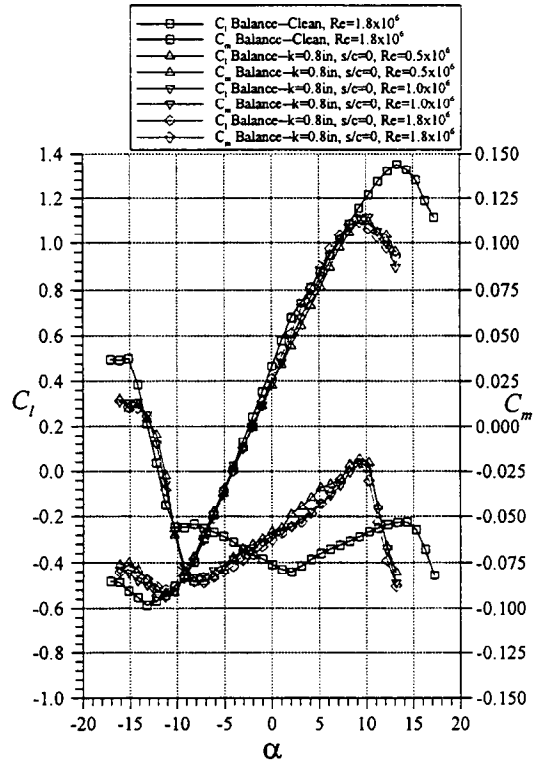**Figure 21:** NLF0414 Clean Airfoil Data at 3 Reynolds numbers

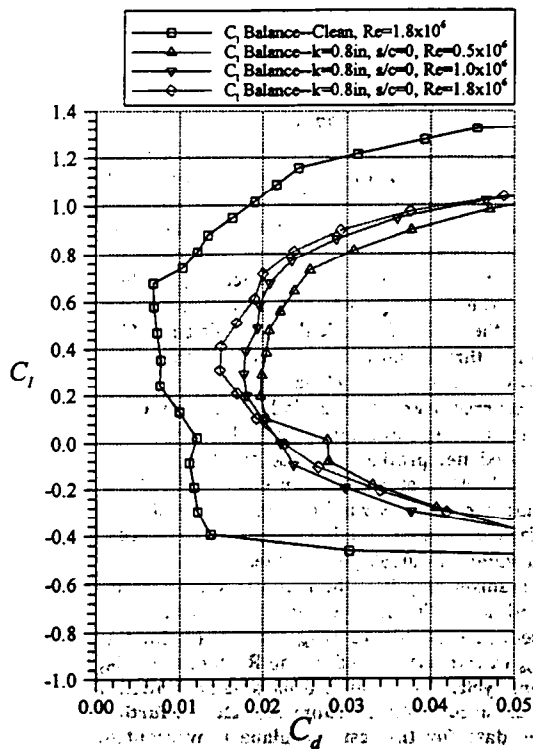**Figure 23:** Reynolds Number Effects on C_l and C_m for r/w = 0.5, s/c = 0% and k = 0.8" shape

390

Figure 24: Reynolds Number Effects on C_d for r/w = 0.5, s/c = 0% and k = 0.8" shape